


Article

Investigation of CO₂ Splitting on Ceria-Based Redox Materials for Low-Temperature Solar Thermochemical Cycling with Oxygen Isotope Exchange Experiments

Daniel Uxa ^{1,*} , Lars Dörner ¹, Michal Schulz ², Nicole Knoblauch ³, Peter Fielitz ¹, Martin Roeb ⁴, Martin Schmücker ^{5,*} and Günter Borchardt ^{1,6}

¹ Institute of Metallurgy, Clausthal University of Technology, 38678 Clausthal-Zellerfeld, Germany

² Institute of Energy Research and Physical Technologies, Clausthal University of Technology, 38640 Goslar, Germany

³ German Aerospace Center, Institute of Materials Research, 51147 Köln, Germany

⁴ German Aerospace Center, Institute of Future Fuels, 51147 Köln, Germany

⁵ Institute of Mechanical Engineering, HRW University of Applied Science, 45479 Mülheim an der Ruhr, Germany

⁶ Clausthal Centre of Material Technology, 38678 Clausthal-Zellerfeld, Germany

* Correspondence: daniel.uxa@tu-clausthal.de (D.U.); martin.schmuecker@hs-ruhrwest.de (M.S.)

Abstract: The surface exchange and bulk transport of oxygen are highly relevant to ceria-based redox materials, which are envisaged for the solar thermochemical splitting of carbon dioxide in the future. Experimental investigations of oxygen isotope exchange on CeO_{2-δ}, Ce_{0.9}M³⁺_{0.1}O_{1.95-δ} (with M³⁺ = Y, Sm) and Ce_{0.9}M⁴⁺_{0.1}O_{2-δ} (with M⁴⁺ = Zr) samples were carried out for the first time utilizing oxygen-isotope-enriched C¹⁸O₂ gas atmospheres as the tracer source, followed by Secondary Ion Mass Spectrometry (SIMS), at the temperature range 300 ≤ T ≤ 800 °C. The experimental \tilde{K}_O and \tilde{D}_O data reveal promising results in terms of CO₂ splitting when trivalent (especially Sm)-doped ceria is employed. The reaction temperatures are lower than previously proposed/reported due to the weak temperature dependency of the parameters \tilde{K}_O and \tilde{D}_O . The majority of isotope exchange experiments show higher values of \tilde{K}_O and \tilde{D}_O for Sm-doped cerium dioxide in comparison to Y-doped and Zr-doped ceria, as well as nominally undoped ceria. The apparent activation energies for both \tilde{K}_O and \tilde{D}_O are lowest for Sm-doped ceria. Using Zr-doped cerium oxide exhibits various negative aspects. The Zr-doping of ceria enhances the reducibility, but the possible Zr-based surface alteration effects and dopant-induced migration barrier enhancement in Zr-doped ceria are detrimental to surface exchange and oxygen diffusion at lower temperatures of T ≤ 800 °C.

Keywords: ceria; oxygen diffusion; oxygen surface exchange; thermochemical cycling; carbon dioxide



Citation: Uxa, D.; Dörner, L.; Schulz, M.; Knoblauch, N.; Fielitz, P.; Roeb, M.; Schmücker, M.; Borchardt, G. Investigation of CO₂ Splitting on Ceria-Based Redox Materials for Low-Temperature Solar Thermochemical Cycling with Oxygen Isotope Exchange Experiments. *Processes* **2023**, *11*, 109. <https://doi.org/10.3390/pr11010109>

Academic Editor: Xiangchao Meng

Received: 22 November 2022

Revised: 19 December 2022

Accepted: 21 December 2022

Published: 30 December 2022



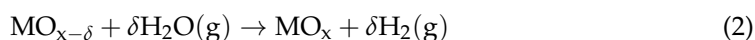
Copyright: © 2022 by the authors. Licensee MDPI, Basel, Switzerland. This article is an open access article distributed under the terms and conditions of the Creative Commons Attribution (CC BY) license (<https://creativecommons.org/licenses/by/4.0/>).

1. Introduction

In order to overcome the global challenges induced by climate change and fossil fuel depletion and the fact that our mobility relies on unsustainable raw materials, great research effort has been focused on the production of hydrogen and synthetic hydrocarbons [1–12]. The solar thermochemical splitting of carbon dioxide and water via two-step redox reactions (solar thermochemical cycling, STCC), utilizing concentrated solar energy and a metal oxide (MO) as a redox material, is generally referred to as a promising path for producing syngas [10]. The STCC process operates at high temperatures and utilizes the entire solar spectrum via the concentration of direct solar radiation with optical point-focusing systems [9]. The two-step redox cycle consists of two thermochemical reactions, a high-temperature endothermic reduction step,



and a low-temperature exothermic re-oxidation step going along with the splitting of water and/or carbon dioxide,



where the non-stoichiometry δ denotes the reduction extent [2,3,5,7,10]. Gradual oxygen release (reduction) or incorporation (re-oxidation) by sub-oxide formation is beneficial for such a thermochemical loop process since virtually no nucleation barrier will affect the redox kinetics. The reduction of the metal oxide occurs at elevated temperatures and low oxygen partial pressure due to the formation of oxygen vacancies in the crystal lattice. The characteristic parameter δ in Equation (1) defining the non-stoichiometry is determined by the applied $T - p_{\text{O}_2}$ conditions and is material specific. The subsequent re-oxidation of the reduced metal oxide in the presence of water vapor or carbon dioxide, according to Equations (2) and (3), causes the splitting reaction. Commonly, the temperature and the gas atmosphere are cycled between the high-temperature reduction step (1) ($T_{\text{reduction}}$ is about 1200–1600 °C) and the low-temperature splitting/re-oxidation step (2–3) ($T_{\text{oxidation}}$ is about 800–1000 °C) [9,10].

Due to its redox thermodynamics and fast redox kinetics, displaying less complex behavior of oxygen non-stoichiometry compared to other oxides of the group AO_2 (with $A = \text{Hf, Pu, Th, U, Zr}$) [13–18], cerium dioxide is a very attractive redox reactive material and was first applied in 2006 for the production of hydrogen, carbon monoxide, and the mixture of both, referred to as syngas [19]. It is now one of the most widely studied fluorite-based oxides [20–27], and currently, most of the research is dealing with ceria as a potential candidate for solar fuel generation via the two-step thermochemical splitting of water and carbon dioxide [1–12]. The thermodynamic properties and the redox kinetics of cerium dioxide can be influenced by doping with additional cationic elements. Here, the term “doping” should not be confused with the notion of doping commonly used in semiconductor physics, as it has the meaning of adding a cationic element M^{y+} into the cationic sublattice of ceria via a suitable metal oxide, resulting in a solid solution with the structure of $\text{Ce}_{1-x}\text{M}_x\text{O}_{2-\delta}$. Ceria is rather substituted than doped. Today’s research has shown comprehensive attempts to modify ceria with di-, tri-, tetra-, and pentavalent dopants to improve the redox performance of ceria. Di- and trivalent dopants cause defects in the crystal structure of ceria that influence the transport properties of oxygen ions as well as the surface reactivity (see, i.e., [28]). However, tetravalent dopants, such as Zr^{4+} and Hf^{4+} , have been shown to improve the redox capacity of ceria [5,7]. In relation to this, the reactive material and its macroscopic and microscopic structure play a decisive role. In general, reactive ceramic bodies in the macroscopic form of beads, foams, or honeycomb structures can be applied [29]. The microscopic structure is that of a sintered solid sample, displaying pores, grain boundaries, and specific grain size. However, important detailed questions, particularly regarding the reaction kinetics, the exact influence of doping elements, the macroscopic structural parameters (powders, granules, foams, honeycomb structures, etc.), the microstructure and porosity of the redox material, as well as the cyclic stability still have to be answered in order to achieve scaling of the redox process at the technical scale.

In general, the redox kinetics of oxides is either controlled by surface exchange reactions or by the bulk transport of oxygen, which includes oxygen diffusion in grains and grain boundaries in the case of a sintered bulk material. The most important prerequisite for the targeted further development of the redox material is the exact knowledge of fundamental parameters such as surface exchange coefficients, K_{O} , and the diffusion coefficients, D_{O} , of oxygen [30,31]. In the case of carbon dioxide splitting, the available data are very fragmented. In addition to the computer simulations of the reaction between CO_2 and CeO_2 based on density functional theory (DFT) (see, i.e., [32] and [33]), there are only a few recent experimental studies on this question. The present work focuses on experimental investigations of ceria in order to minimize the existing data gap (K_{O} , D_{O}),

with carbon dioxide reduction as a focus, being one of the two essential steps toward the solar thermochemical production of syngas. The most direct method of measuring oxygen diffusivities and surface exchange coefficients in oxides is oxygen isotope exchange followed by Secondary Ion Mass Spectrometry (SIMS) depth profiling (IEDP) or cross-section line scan (IELS). By utilizing oxygen isotope enriched $C^{18}O_2$ gas atmospheres, this well-established approach represents the core of the experimental work of this study. Important aspects such as surface reaction with carbon dioxide reduction in comparison to the oxygen exchange reaction, phenomenological description (K_O , D_O) and the interpretation of the rate constants, diffusion in chemical non-equilibrium, the influence of the doping elements as well as the influence of the respective kinetic regime are discussed.

2. Materials and Methods

2.1. Sample Preparation

CeO_2 and doped $Ce_{0.9}M^{3+/4+}_{0.1}O_{2-x}$ (with $M^{3+/4+} = Y, Sm, Zr$) powders were synthesized as described elsewhere [30,31], using the Pechini method [34], a citric-acid-assisted combustion method. Therefore, $Ce(NO_3)_3 \cdot 6H_2O$ (Alfa Aesar, 99.99%) and salts of doping Elements Zr, Sm and Y ($ZrO(Cl)_2 \cdot 8H_2O$, $Sm(NO_3)_3 \cdot 6H_2O$, $Y(NO_3)_3 \cdot 6H_2O$, 99.9%, Alfa Aesar) were dissolved in demineralized water in the corresponding concentrations and citric acid (VWR chemicals) and ethylene glycol (VWR chemicals) were added in a molar ratio of 1:2:3 (cations: citric acid: ethylene glycol). The obtained mixture was stirred at $T = 100^\circ C$ for $t = 1$ h. A stepwise increase in the temperature up to $T = 200^\circ C$ resulted in a concentrated solution due to gradual water evaporation. Finally, a viscous yellow gel was formed by polyesterification. This gel was heated to $T = 450^\circ C$ for the pyrolysis of any organic species. The product was calcined in an electrical furnace at $T = 800^\circ C$ in ambient air for $t = 2$ h to remove any remaining carbonaceous species. The obtained oxide powder was analyzed by using X-ray diffractometry (XRD) (D-5000, Siemens) using Ni-filtered $Cu-K\alpha$ radiation. The CaF_2 -type CeO_2 phase was identified. Inductively coupled plasma optical emission spectrometry (ICP-OES) was performed to reveal the impurity concentration. The results are summarized in Table 1. While the concentration of lanthanum (about 0.2 wt-%) must be considered as a trivalent dopant, the other impurities were below 0.09 wt-% in total.

Table 1. Compilation of the ICP-OES analysis of a sintered CeO_2 pellet.

Element	Concentration/ppm
La	1910
Zr	358
Pr	217
Ca	110
Nd	99
Mg	63
Nb	48
Fe	44
Na	192
Ga, Cr, K, Li, Sm, Y	<25

In order to prepare disc-shaped pellets, the powder was milled using a laboratory ball mill (planetary micromill Pulverisette 7, Fritzsche, for $t = 3 \times 10$ min, with 500 rpm and a mass ratio of 1:10:60 powder:isopropyl alcohol: ZrO_2 balls) and uniaxially cold-pressed at $p = 283$ MPa. After sintering at $T = 1650^\circ C$ for $t = 2$ h the pellets were characterized using scanning electron microscopy (SEM, Ultra 55 FEG Carl Zeiss, Germany) and had a relative density of about 95% and an average grain size of about 20 μm (Figure 1). The samples were embedded in a cold-curing embedding agent (Technovit 5071, Kulzer) and polished with water-based diamond suspensions of 15, 6, 3, and 1 μm particle sizes. Then, the embedding agent was dissolved in acetone. The samples were cleaned with isopropanol and annealed. In order to prepare the samples for SIMS IELS measurements, they were newly embedded

(Technovit 5071, Kulzer), cut, and dissolved again with acetone. Thereafter, the samples were inversely mounted (see Section 1, Figures S1 and S2 in the Supplementary Material, as well as references [35–37], for more details), cold-embedded (EPO-FIX, Struers), and prepared as described above.

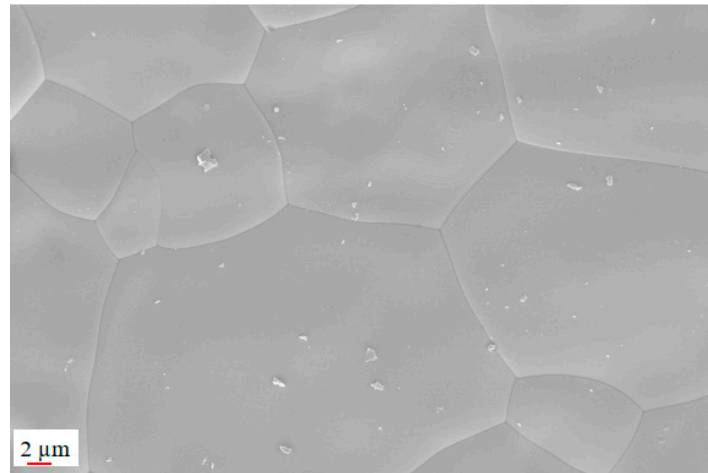


Figure 1. SEM image of a sintered CeO_2 pellet with a grain size of about $20\ \mu\text{m}$ and a relative density of 95%.

2.2. Experimental Setup for Isotope Exchange Utilizing C^{18}O_2

The cut, polished, and cleaned (ultrasonic cleaning in acetone followed by isopropanol) CeO_2 and doped $\text{Ce}_{0.9}\text{M}^{3+/4+}_{0.1}\text{O}_{2-x}$ (with $\text{M}^{3+/4+} = \text{Y}, \text{Sm}, \text{Zr}$) samples were annealed in a self-constructed experimental setup with an IR radiation heated furnace (Quad Elliptical, RI Controls/Research Incorporated), which allows fast heating rates of up to $100\ \text{K/s}$ in the temperature range of $300\ ^\circ\text{C} \leq T \leq 900\ ^\circ\text{C}$. The samples were placed on a coarse platinum mesh (avoiding contact of the platinum with the polished sample surface) in a quartz holder in well-defined atmosphere conditions (vacuum down to 10^{-9} bar, purified argon gas flow with $p_{\text{O}_2} \leq 10^{-25}$ bar, oxygen isotope enriched gas mixture or other gas atmospheres being used), as shown in Figure 2. The oxygen partial pressure during re-oxidation experiments with CO_2 is much lower in comparison to established experimental work using pure oxygen. The p_{O_2} is controlled by the $\text{CO}:\text{CO}_2$ ratio of the given gas mixture, by the respective temperature T and/or additional oxygen sources.

Because of the considerable cost of C^{18}O_2 gas (835 ppm CO, < 250 ppm O_2 , Campro Scientific), a gas mixture of purified argon with “labelled” carbon dioxide with an $\text{Ar}:\text{C}^{18}\text{O}_2$ ratio of 10:1 in a closed volume ($V = 1\ \text{l}$) was used for the experimental work. In the general case of measurements with a chemical potential gradient (difference in the chemical potential of oxygen) at the gas/solid interface, the experimental work starts with a reduction step of the samples utilizing purified argon gas, where the respective oxygen non-stoichiometry δ of the sample depends on the temperature of the reduction step and the doping elements and was estimated based on the data in the literature [38,39] (for example, the δ of $\text{CeO}_{2-\delta}$ is estimated to be 0.2 for $T_{\text{red}} = 800\ ^\circ\text{C}$ and $p_{\text{O}_2} = 10^{-24}$ bar). For the re-oxidation experiments, the starting oxygen activity of the reduced ceria samples has to be lower than the oxygen activity of the $\text{Ar}/\text{C}^{18}\text{O}_2$ gas mixture in which the samples are annealed at a given temperature: $\mu_{\text{O}_2}^{\text{sample}} < \mu_{\text{O}_2}^{\text{gas}}$.

During the experiment, the ^{18}O isotope will be incorporated from the C^{18}O_2 gas into the sample bulk. Because of the closed volume (continuous gas flow was not used due to the limited amount of C^{18}O_2 gas), the gradient of the chemical potential of oxygen between the gas phase and the solid sample will change during the experiment for two reasons. First, the oxygen activity in the sample will increase, especially at the sample surface and in the near-surface region of the bulk, due to oxygen incorporation. Second, the oxygen uptake of the samples will decrease the oxygen partial pressure in the gas phase. The oxygen partial

pressure of the $\text{Ar}/\text{C}^{18}\text{O}_2$ gas mixture was measured for all experiments with a lambda probe, which enabled the estimation of the oxygen activity of the sample at the end of the exchange experiment (see [31] for more details). The experimental conditions for the reduction step and isotope exchange step with the respective parameters are summarized in Table 2.

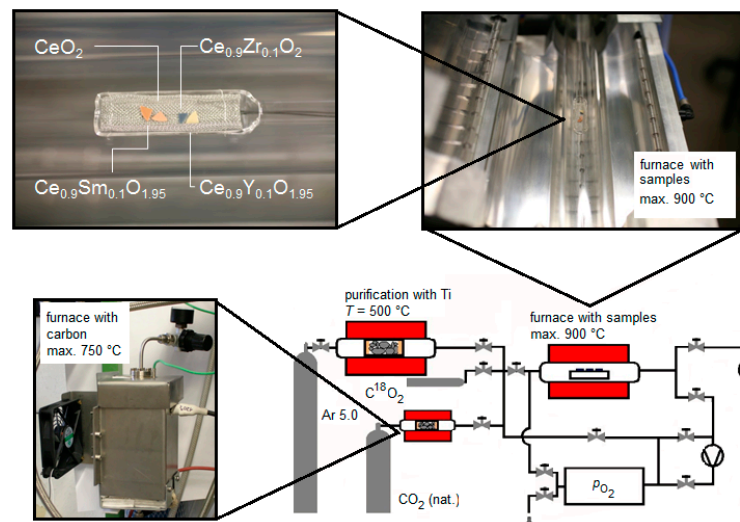


Figure 2. Overview display of the self-constructed experimental setup with an IR radiation heated furnace which allows fast heating rates up to 100 K/s in the temperature range between $T = 300\text{ }^{\circ}\text{C}$ and $T = 900\text{ }^{\circ}\text{C}$. Further can be seen in the purification unit where the argon gas flow is reduced by a titanium sponge at $T = 500\text{ }^{\circ}\text{C}$, which enables oxygen partial pressures for the reduction step of $p_{\text{O}_2} \leq 10^{-24}\text{ bar}$, as well as an additional carbon furnace which allows control of the $\text{CO}:\text{CO}_2$ ratio of the given gas mixture. The oxygen partial pressure was measured for all experiments in situ with a lambda probe (further details are given in the text).

Table 2. Compilation of the experimental conditions and parameters as used in this work.

Reduction Step	Isotope Exchange with C^{18}O_2 Gas
Ar	$\text{Ar}/\text{C}^{18}\text{O}_2$ (10:1)
$T_{\text{reduction}} \geq T_{\text{experiment}}$	$T = T_{\text{experiment}}$
$p_{\text{total}} = 1\text{ bar}$	$p_{\text{total}} = 1\text{ bar}$
$10^{-23} \leq p_{\text{O}_2} \leq 10^{-25}\text{ bar}$	$p_{\text{O}_2} \leq 10^{-12}\text{ bar}$

2.3. Secondary Ion Mass Spectrometry and Analysis

A detailed overview of the applied SIMS methods and techniques used in this work can be found in the Supplementary Material in Section 2, Figures S3 and S4, as well as in references [40–42]. SIMS IELS measurements were conducted (a) using a SIMS Workstation (Hidden Analytical Ltd) with positive 10 keV argon ions as the primary beam with a 100 nA ion current and a spot size of about $50 \times 110\text{ }\mu\text{m}^2$; the raster-scanned area was $500 \times 500\text{ }\mu\text{m}^2$ in the imaging mode; negative secondary ions were used for the analysis of the samples, and sample charging was prevented by an electron flood gun; (b) using an IMS 7f N (CAMECA) with a positive 15 keV cesium ion primary beam with a (10–15) nA ion current and a raster of $(50\text{--}500)\text{ }\mu\text{m}$ in the imaging mode. The SIMS IEDP measurements were carried out using an IMS 3f/4f (CAMECA) with negative 15 keV oxygen ions as the primary beam with a 100 nA ion current. The raster-scanned area was $250 \times 250\text{ }\mu\text{m}^2$, and the area of the analyzed zone was $60 \times 60\text{ }\mu\text{m}^2$. Positive secondary ions were used for the analysis of the samples. Sample charging was partially prevented by sputtering a thin layer of gold (about 20 nm) on top of the sample surface. Depth calibration was performed by measuring the SIMS crater depth using a surface profiler (Alpha Step 500, Tencor). The analysis of the measured SIMS depth profiles (^{18}O fraction depth profiles) was undertaken, as explained in Section 3.1 and in the Supplementary Material in Section 2.

3. Results and Discussion

3.1. Oxygen Exchange from $C^{18}O_2$ Atmospheres at $300\text{ }^{\circ}\text{C} \leq T \leq 800\text{ }^{\circ}\text{C}$

Comparable to the low-temperature step of the two-step thermochemical cycle for splitting CO_2 , the experimental work utilizing a chemical potential gradient (difference in the chemical potential of oxygen) at the gas/solid interface starts with reduced (doped or un-doped) ceria samples, with the respective oxygen non-stoichiometry of the sample depending on the temperature of the reduction step and the sample type (refer Table 2). During the experiment, the ^{18}O released from $C^{18}O_2$ will be incorporated into the sample bulk. Figure 3 shows a typical SIMS line scan profile for the ^{18}O distribution of a 10 at-% Zr-doped ceria sample after an oxygen isotope exchange from $C^{18}O_2$ ($Ar/C^{18}O_2$ gas mixture) under non-equilibrium conditions at $T = 700\text{ }^{\circ}\text{C}$ for $t = 10\text{ min}$. The analytical solution of the diffusion problem in a semi-infinite homogeneous media, as given by Crank [40], was proposed in a more specific notation by Fielitz and Borchardt [35]:

$$\frac{c_{^{18}O}(x,t) - c_{^{18}O}^{\infty}}{c_{^{18}O}^s - c_{^{18}O}^{\infty}} = \text{erfc}\left(\frac{x}{\sigma}\right) - \exp\left(2\frac{x}{\sigma}\sqrt{\frac{t}{\tau}} + \frac{t}{\tau}\right) \text{erfc}\left(\frac{x}{\sigma} + \sqrt{\frac{t}{\tau}}\right) \quad (4)$$

with $\sigma \equiv 2\sqrt{Dt}$ and $\tau \equiv \frac{D}{K^2}$

where $c_{^{18}O}^{\infty}$ is the natural abundance of ^{18}O in the sample (at $x \rightarrow \infty$), σ is the diffusion length of the tracer isotope, and τ is the characteristic time constant that determines the duration that is necessary to reach equilibrium between the ^{18}O gas concentration and the ^{18}O concentration at the surface of the solid. The simultaneous determination of (chemical) oxygen diffusivity and (chemical) oxygen surface exchange coefficient is established by measuring the depth distribution of the atomic fraction of ^{18}O and fitting it with Equation (4). The result is shown in Figure 3 together with the fit curve, and the resulting parameters are summarized in the inset of Figure 3. Note that (chemical) coefficients for oxygen diffusion and oxygen surface exchange that were determined under the conditions of an oxygen potential gradient ($\Delta\mu_{O_2} \neq 0$) are labeled by a tilde: \tilde{D}_O , \tilde{K}_O . The determined (chemical) oxygen diffusion coefficients \tilde{D}_O and oxygen surface exchange coefficients \tilde{K}_O in ceria containing 10 at-% of dopants (Y, Sm, Zr) and in nominally un-doped ceria samples in the temperature range of $300\text{ }^{\circ}\text{C} \leq T \leq 800\text{ }^{\circ}\text{C}$ are shown in Figures 4 and 5, together with the calculated activation enthalpies.

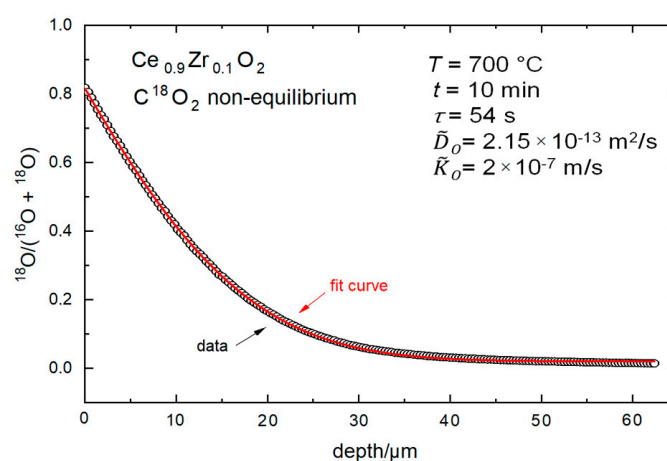


Figure 3. SIMS line-scan depth profile for the ^{18}O distribution of a 10 at-% Zr-doped ceria sample after an oxygen isotope exchange from $C^{18}O_2$ ($Ar/C^{18}O_2$ gas mixture) in non-equilibrium conditions at $T = 700\text{ }^{\circ}\text{C}$. The oxygen isotope fraction is shown in comparison with the fit by Equation (3), together with the simultaneous determined non-equilibrium (chemical) values \tilde{D}_O and \tilde{K}_O .

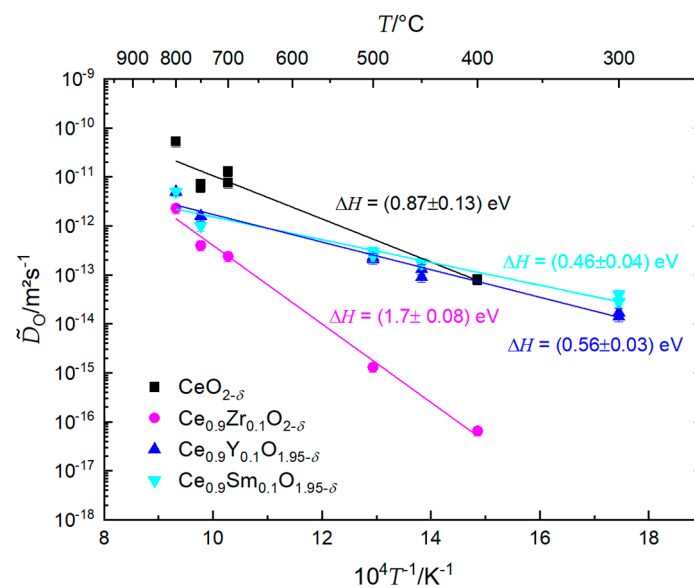


Figure 4. Determined chemical oxygen diffusion coefficients \tilde{D}_O in ceria containing 10 at-% of dopants (Y, Sm, Zr) and in nominally un-doped ceria samples in the temperature range from $T = 300$ °C to $T = 800$ °C, together with calculated activation enthalpies.

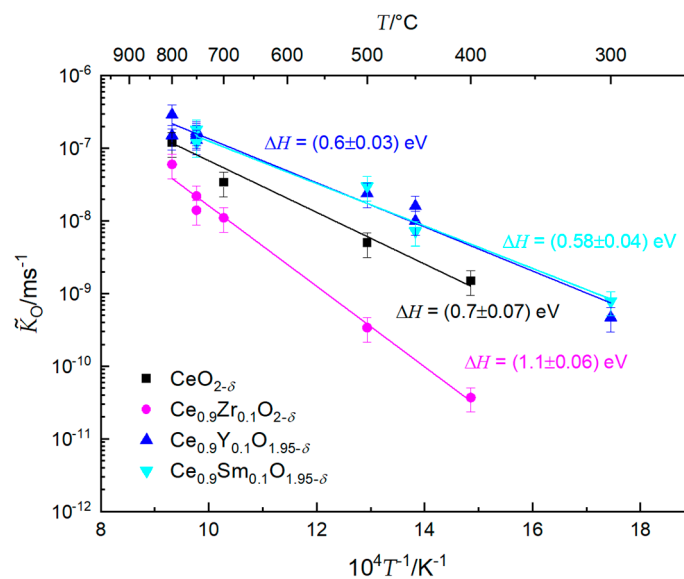


Figure 5. Determined chemical oxygen exchange coefficients \tilde{K}_O in ceria containing 10 at-% of dopants (Y, Sm, Zr) and in nominally un-doped ceria samples in the temperature range from $T = 300$ °C to $T = 800$ °C, together with calculated activation enthalpies.

3.2. Simultaneous Determination of \tilde{D}_O and \tilde{K}_O and Estimation of the Kinetic Regime by \tilde{K}_O/\tilde{D}_O Data

The redox kinetics of ceria are either controlled by surface exchange reactions or by the bulk transport of oxygen. In the mixed kinetic regime, the observed kinetics of the reduction/oxidation process are influenced by the contributions of both parameters \tilde{K}_O and \tilde{D}_O . A deeper insight into mechanisms and kinetics of ceria reduction and re-oxidation with respect to the derived \tilde{K}_O/\tilde{D}_O data is given by calculating the characteristic dimensionless parameter of the kinetic regimes L with $L = \frac{h}{2} \frac{\tilde{K}_O}{\tilde{D}_O}$ and h = sample thickness (in our case 1 mm), as discussed in [30]. In Figure 6, the derived \tilde{K}_O/\tilde{D}_O data sets from Section 3.1 are given for the respective temperature range, together with the calculated regime boundaries. The data reveal that non-equilibrium oxygen isotope exchange falls either into the diffusion-

controlled range or in the mixed kinetic regime if the condition $T \leq 800$ °C is given (if the sample thickness is about 1 mm). The \tilde{K}_O/\tilde{D}_O ratios tend to shift from the diffusion-controlled regime to the mixed regime with increasing temperature. The data extrapolation suggests that the surface exchange-controlled regime could be reached at temperatures well above 900 °C. These findings coincide with the results published by Knoblauch et al. [30], who discussed a surface-controlled kinetic regime at higher temperatures $T \geq 1300$ °C for nominally undoped ceria (polycrystalline CeO_2 of 1 mm thickness) that was investigated using thermogravimetric analysis in non-equilibrium conditions. In addition to that, Manning et al. [43] reported a surface-controlled kinetic regime for Gd-doped ceria already in the temperature range $T \leq 1100$ °C. This was attributed to the fact that the trivalent dopant increases the concentration of oxygen vacancies and hence the diffusivity of oxygen rather than surface exchange kinetics.

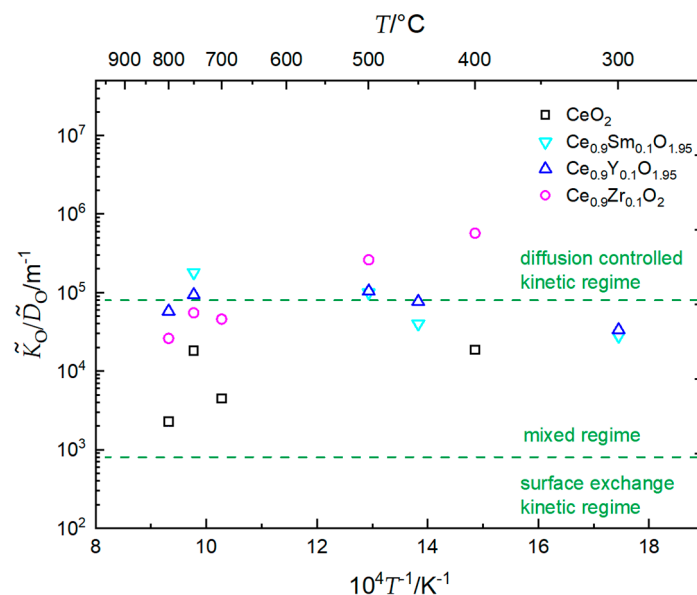


Figure 6. Calculated \tilde{K}_O/\tilde{D}_O ratios for non-equilibrium oxygen isotope exchange from C^{18}O_2 together with the calculated regime boundaries in the temperature range from $T = 300$ °C to $T = 800$ °C for ceria containing 10 at-% of dopants (Y, Sm, Zr) and in nominally un-doped ceria samples. The boundaries for the kinetic regime were calculated according to $L = \frac{h}{2} \frac{K}{D}$ with $h = 1$ mm and L being the characteristic dimensionless parameter of the kinetic regimes [30,35].

As discussed in [35], the simultaneous determination of oxygen diffusivity and surface exchange coefficient works well only in a certain window of experimental parameters, confined by feasible diffusional distances ($30 \text{ nm} < \sigma < 0.5 \text{ mm}$) and dwell times (seconds to years). Utilizing Equation (3) with the parameters discussed by Fielitz and Borchardt [35], an accessible K - D window for the simultaneous determination of \tilde{D}_O and \tilde{K}_O can be derived (Figure 7). The lines define a range of experimental parameters where a simultaneous determination is possible with acceptable errors.

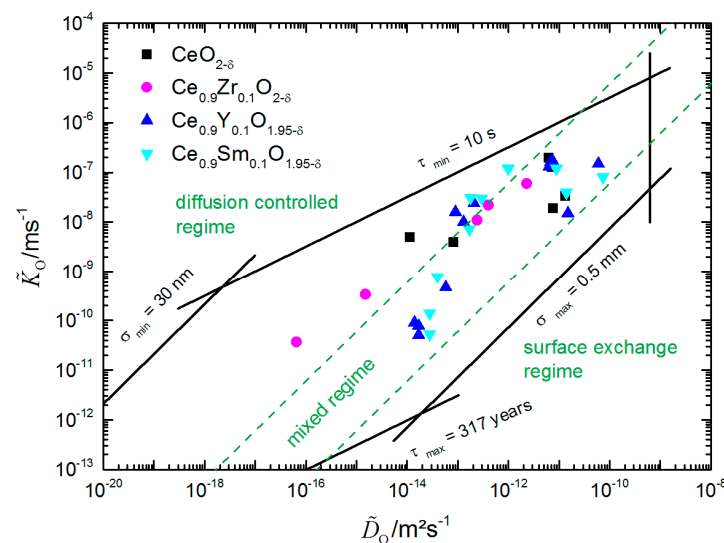
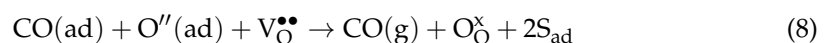
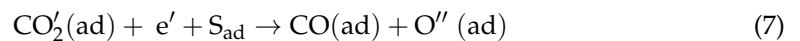


Figure 7. The accessible K - D window plotted partially together with K - D -Data derived in non-equilibrium experimental conditions in the temperature range $T = 300\text{ }^{\circ}\text{C}$ to $T = 800\text{ }^{\circ}\text{C}$ utilizing C^{18}O_2 . Additionally, the boundaries for the kinetic regime are drawn [30,35].

3.3. Reaction Model for CO_2 Splitting on Reduced $\text{CeO}_{2-\delta}$ Surfaces and Derivation of the Equilibrium Exchange Rate of Oxygen

The surface reaction of oxygen incorporation is made up of several complex individual steps [44,45]. The reaction pathway involves the adsorption and dissociation of oxygen molecules on the surface, the reaction with an oxygen vacancy and the transfer of oxygen ions through the surface, in addition to several charge transfer steps. The most likely rate-determining step (rds) of the reaction pathway is charge transfer leading to dissociation [45]. According to Bodenstein's principle, one step in the pathway is assumed to be rate-determining and all of the preceding and succeeding reaction steps are treated as being at quasi-equilibrium. As CO_2 splitting on reduced $\text{CeO}_{2-\delta}$ surfaces involves the exchange and incorporation of oxygen, it is expedient to consider the oxygen incorporation as a fundamental reaction, as discussed by Schaube et al. [46]. In accordance with the discussed established ideas on surface exchange from pure oxygen atmospheres, the following reaction scheme utilizing Kröger-Vink notation [47] can be deduced [31]:



where S_{ad} represents a CO_2 surface adsorption site. Investigations showed the high surface concentration and the high stability of the reactive surface Ce^{3+} ions over a wide range of temperatures and of oxygen partial pressures on ceria [48,49]. Currently, Ce^{3+} ions and oxygen vacancies $\text{V}_{\text{O}}^{\bullet\bullet}$ are believed to be the active sites on ceria surfaces. This reaction path represents the most simplified possibility as reaction intermediates such as carbonate species (CO_3^{2-}) [28,50–52] are not considered here.

The so-called apparent or effective equilibrium exchange rate of oxygen $\mathfrak{R}_{\text{O}}^0$ (being a measure of the dynamics at equilibrium, which is likewise an exchange current density) of the rate-determining step is then defined as follows:

$$\mathfrak{R}_{\text{O}}^0 = \left(\overset{\leftarrow}{k}_{\text{rds}} [\text{CO}'_{2,\text{ad}}] \times \vec{k}_{\text{rds}} [\text{CO}_{2,\text{ad}}] [e'] \right)^{\frac{1}{2}} \quad (9)$$

where \vec{k}_{rds} and $\overleftarrow{k}_{\text{rds}}$ are again the forward and backward reaction rates of the rate-determining charge transfer step. After inserting the mass action constants for the preceding and succeeding reaction steps (adsorption and incorporation):

$$K_{\text{ad}} = \frac{[\text{CO}_{2,\text{ad}}]}{[\text{CO}_2]} \quad (10)$$

$$K_{\text{inc}} = \frac{[\text{CO}][\text{O}_\text{O}^\times]}{[\text{CO}'_{2,\text{ad}}][\text{V}_\text{O}^{\bullet\bullet}][e']} \quad (11)$$

as well as the mass action constant for the carbon dioxide dissociation in the gas phase,

$$K_{\text{diss}} = \frac{[\text{CO}]p_{\text{O}_2}^{\frac{1}{2}}}{[\text{CO}_2]} \quad (12)$$

into Equation (9) one can finally deduce:

$$\mathfrak{R}_\text{O}^0 = \left(\frac{\overleftarrow{k}_{\text{rds}} \vec{k}_{\text{rds}} K_{\text{ad}} K_{\text{diss}}}{K_{\text{inc}}} \right)^{\frac{1}{2}} \frac{[\text{CO}_2] ([\text{O}_\text{O}^\times])^{\frac{1}{2}}}{[\text{V}_\text{O}^{\bullet\bullet}]^{\frac{1}{2}} p_{\text{O}_2}^{\frac{1}{4}}} \quad (13)$$

Since this empirical expression suggests that

$$\mathfrak{R}_\text{O}^0 \sim \frac{[\text{CO}_2] ([\text{O}_\text{O}^\times])^{\frac{1}{2}}}{[\text{V}_\text{O}^{\bullet\bullet}]^{\frac{1}{2}} p_{\text{O}_2}^{\frac{1}{4}}} \quad (14)$$

the p_{O_2} and $[\text{V}_\text{O}^{\bullet\bullet}]$ dependency of \mathfrak{R}_O^0 with regard to the experimental conditions of oxygen exchange from CO_2 can be discussed in more detail. In the reduced and, therefore, significantly non-stoichiometric ceria samples, the high concentration of oxygen vacancies limits the influence of the structural oxygen vacancies related to tri- or divalent dopants. As \mathfrak{R}_O^0 also depends on the oxygen partial pressure of the surrounding gas atmosphere, the $T - a_{\text{O}_2}$ relation (for example $a_{\text{O}_2} = 10^{-15}$ at $T = 700^\circ\text{C}$ and $a_{\text{O}_2} = 10^{-12}$ at $T = 800^\circ\text{C}$), as discussed in a previous publication [31], has the strongest influence and controls in non-equilibrium conditions the exchange rate of oxygen. For a comprehensive understanding, the normalized exchange rate \mathfrak{R}_O^0 of the rate-determining step in the reaction sequence is calculated utilizing the $\tilde{K}_\text{O}/\tilde{D}_\text{O}$ data sets and Equation (15) for the case of mixed or diffusion-controlled kinetic regimes [53]:

$$K_\text{O}^{h \rightarrow \infty} = \left(w_\text{O}(x=0) D_\text{O} \frac{\mathfrak{R}_\text{O}^0}{c_\text{O}(x=0)} \right)^{\frac{1}{2}} \quad (15)$$

In Figure 8 the derived data for oxygen isotope exchange from C^{18}O_2 are given for the respective temperature range from $300^\circ\text{C} \leq T \leq 800^\circ\text{C}$ together with the calculated activation enthalpies, with $\mathfrak{R}_\text{O}^0 w_\text{O}(x=0)/c_\text{O}(x=0) = (\tilde{K}_\text{O})^2/\tilde{D}_\text{O}$, where c_O and w_O are the concentration and the thermodynamic factor of oxygen near the surface.

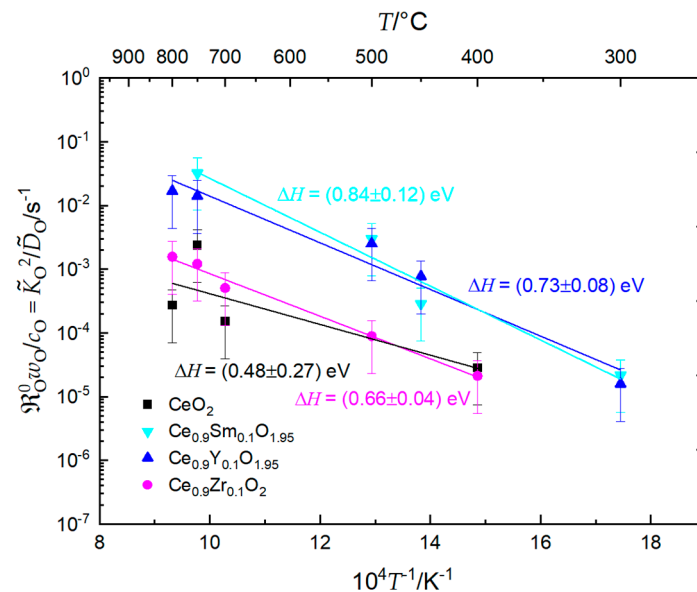


Figure 8. Calculated normalized exchange rates $\mathcal{R}_{\text{OwO}}^0(x=0)/c_{\text{O}}(x=0) = (\tilde{K}_{\text{O}})^2/\tilde{D}_{\text{O}}$ for non-equilibrium oxygen isotope exchange from C^{18}O_2 for ceria containing 10 at-% of dopants (Y, Sm, Zr) and in nominally un-doped ceria samples in the temperature range from $T = 300^\circ\text{C}$ to $T = 800^\circ\text{C}$, together with calculated activation enthalpies.

3.4. Discussion of the Oxygen Exchange Kinetics Considering the Determined Apparent Activation Enthalpies

In general, the calculated overall activation enthalpies for the chemical diffusion of oxygen for trivalent-doped and nominally undoped ceria of (0.46 ± 0.04) eV, (0.56 ± 0.03) eV, and (0.87 ± 0.13) eV represent the oxygen ion migration energy ΔH_{m} . Compared to the low-temperature regime ($T < 1000^\circ\text{C}$) of oxygen tracer diffusivity in ceria-based samples, as published earlier [31], the determined activation enthalpies of nominally undoped ceria and Sm-doped ceria are lower for chemical diffusion, which suggests a dependency of ΔH_{m} on the oxygen vacancy concentration of the reduced samples. This is attributed to the lattice expansion of the ceria crystal upon reduction, where, according to Muhich [54], the outward expansion of the cations neighbouring the oxygen vacancy caused by non-counterpoised forces induces long-range structural distortions.

The calculation of ΔH for non-equilibrium oxygen diffusivity of 10 at-% Zr-doped ceria in the low-temperature region yields, in comparison, an increased value of (1.7 ± 0.08) eV, despite the high oxygen vacancy concentration in the solid. Regarding this finding, defect interactions must be discussed. It is known from the theoretical calculations performed by Grieshammer et al. [55,56] that in Zr-doped ceria a strong solute–vacancy attraction occurs between Zr^{4+} ions and oxygen vacancies, which is due to the small size of the zirconium ion, allowing favorable relaxation around the oxygen vacancy. Thus, according to Grieshammer et al., there are three reasons affecting oxygen diffusion in Zr-doped ceria, which are the trapping of oxygen vacancies by dopant ions, the blocking effect, which alters the migration barriers around the defects, and the lattice contradiction due to Zr-doping. Furthermore, Eufinger et al. [57] showed experimentally that the conductivity in Y-doped ceria is significantly decreased by Zr-doping. The experimental findings on the oxygen diffusivity of this work also suggest a higher migration barrier in Zr-doped ceria resulting from dopant–vacancy interactions.

The calculated activation enthalpies for chemical oxygen diffusivity for trivalent-doped and nominally undoped ceria differ by 0.41 eV and 0.29 eV, respectively, which was not found for oxygen tracer diffusion in an earlier study [31]. In this study, the effects of the high oxygen vacancy concentrations on the bulk transport properties must be considered, as isolated defects can interact to form defect complexes, especially if the

vacancy concentration is high. Bishop et al. discussed various defect complexes that can potentially form and found isolated defects and intrinsic trimers composed of reduced cations and oxygen vacancies in the form of $(\text{Ce}'_{\text{Ce}}\text{V}_{\text{O}}^{\bullet\bullet}\text{Ce}'_{\text{Ce}})^{\times}$ to be the most significant species [58,59]. A comparison of $\text{CeO}_{2-\delta}$ and $\text{Ce}_{0.9}\text{Gd}_{0.1}\text{O}_{1.95-\delta}$ by the cited authors showed differences in the chemical expansion as a function of p_{O_2} , which is explained by an increased tendency of undoped ceria to form defect complexes, changing the ratio of defect complexes to isolated defects. At a non-stoichiometry of $\delta = 0.15$, undoped ceria exhibits a calculated intrinsic trimer fraction of 86%, whereas 10 at-% Gd-doped ceria exhibits an intrinsic trimer fraction of 62%, having a higher fraction of isolated defects. Based on the current knowledge, it can be speculated that intrinsic trimers influence the ionic transport by trapping the oxygen vacancy itself and by the alteration of the migration barriers around the defect complex.

The determined \tilde{K}_{O} data for nominally undoped and trivalent-doped ceria also shows only weak temperature dependence in contrast to higher $\Delta H_{\text{a}}^{\tilde{K}_{\text{O}}}$ values for the Zr-doped ceria. Previously reported findings on surface alteration effects under low-oxygen partial pressure and high temperatures [31] can explain the observed differences. The selective surface evaporation of ceria, whose vapor pressure is considerably higher than that of zirconia, and segregation of zirconia can lead to a porous surface zone in the $\text{Ce}_2\text{Zr}_2\text{O}_7$ pyrochlore and, consequently, to a surface enrichment of zirconia. Zr-doped ceria that is slightly different in its composition and surface structure might induce significant differences in oxygen surface exchange, leading to a different value of $\Delta H_{\text{a}}^{\tilde{K}_{\text{O}}}$. A comparison can be made to the \tilde{K}_{O} data obtained in the true exchange-controlled kinetic regime, as the $\tilde{K}_{\text{O}}/\tilde{D}_{\text{O}}$ ratios of this work suggest a diffusion-controlled or mixed kinetic regime at $T \leq 800$ °C, as discussed in Section 3.2. Knoblauch et al. [30] discussed surface exchange-controlled reduction kinetics at higher temperatures of $T \geq 1300$ °C for nominally undoped CeO_2 (polycrystalline CeO_2 samples of 1 mm thickness) using thermogravimetric analysis in non-equilibrium conditions, and found that \tilde{K}_{O} shows virtually no temperature-dependency.

The influence of the kinetic regime on the apparent activation enthalpy of the surface exchange coefficient was later thoroughly discussed by Fielitz and Borchardt [53]. They suggest that the measured oxygen surface exchange coefficient, if measured in the mixed regime and in the diffusion controlled kinetic regime, depends not only on the equilibrium oxygen exchange rate at the gas/solid interface but also on the oxygen diffusion coefficient in the bulk (the reader is referred to Section 3 of the Supplementary Material for a full discussion on the correlation between K_{O} and D_{O}). As a consequence, apparent $\Delta H_{\text{a}}^{\tilde{K}_{\text{O}}}$ data are the mean values of the individual activation enthalpies $\Delta H_{\text{a}}^{\tilde{D}_{\text{O}}}$ and $\Delta H_{\text{a}}^{\mathfrak{R}_{\text{O}}^0}$ in case sufficiently thick samples were employed. According to this theory, $\Delta H_{\text{a}}^{\mathfrak{R}_{\text{O}}^0}$ can be estimated by the relation $\Delta H_{\text{a}}^{\mathfrak{R}_{\text{O}}^0} = 2\Delta H_{\text{a}}^{\tilde{K}_{\text{O}}} - \Delta H_{\text{a}}^{\tilde{D}_{\text{O}}}$, which is shown in Table 3. The values range between 0.5 eV and 0.7 eV, which is in good agreement with the calculated activation enthalpies of the normalized exchange rates in Figure 8 within the experimental errors.

Table 3. Calculated values of the apparent activation enthalpy of the oxygen exchange rate $\mathfrak{R}_{\text{O}}^0$ with regard to the relation $\Delta H_{\text{a}}^{\mathfrak{R}_{\text{O}}^0} = 2\Delta H_{\text{a}}^{\tilde{K}_{\text{O}}} - \Delta H_{\text{a}}^{\tilde{D}_{\text{O}}}$.

Sample Type	$\Delta H_{\text{a}}^{\tilde{K}_{\text{O}}}/\text{eV}$	$\Delta H_{\text{a}}^{\tilde{D}_{\text{O}}}/\text{eV}$	$\Delta H_{\text{a}}^{\mathfrak{R}_{\text{O}}^0} = (2\Delta H_{\text{a}}^{\tilde{K}_{\text{O}}} - \Delta H_{\text{a}}^{\tilde{D}_{\text{O}}})/\text{eV}$
$\text{CeO}_{2-\delta}$	0.7	0.87	0.53
$\text{Ce}_{0.9}\text{Zr}_{0.1}\text{O}_{2-\delta}$	1.1	1.7	0.5
$\text{Ce}_{0.9}\text{Sm}_{0.1}\text{O}_{1.95-\delta}$	0.58	0.46	0.7
$\text{Ce}_{0.9}\text{Y}_{0.1}\text{O}_{1.95-\delta}$	0.6	0.56	0.64

Concerning the temperature dependency of the normalized exchange rate $\mathfrak{R}_{\text{O}}^0$, the contribution of w_{O} and c_{O} to $\Delta H_{\text{a}}^{\mathfrak{R}_{\text{O}}^0}$ must also be considered as both parameters strongly depend on the oxygen non-stoichiometry δ . Based on the work of Claus et al. [60] who

provided a relation of $w_O = \frac{3c_O}{[V_{O^{\bullet\bullet}}]}$, it is possible to deduce that $\frac{w_O}{c_O} = \frac{\text{const.}}{n\delta(T)}$. As a first approximation, one can assume that the temperature dependencies of c_O and w_O compensate each other, but there will remain a contribution to $\Delta H_a^{\text{app}} O$ that cannot be expressed in quantitative terms by $\Delta H_a^{\tilde{D}O}$ and $\Delta H_a^{\tilde{K}O}$ in the context of this work.

4. Conclusions

The experimental work shows promising results regarding CO₂ splitting using trivalent-doped ceria, especially Sm-doped ceria, at lower temperatures than previously suggested for the splitting/re-oxidation step. Several findings indicate the positive influence of doping ceria with trivalent dopants, especially Sm. The majority of isotope exchange experiments under the various experimental conditions show enhanced values of \tilde{D}_O and \tilde{K}_O for 10 at-% Sm-doped cerium dioxide in comparison to 10 at-% Y-doped and Zr-doped as well as nominally undoped ceria. The lowest apparent activation energies for both, \tilde{D}_O and \tilde{K}_O , were observed in case of 10 at-% Sm-doped ceria. Considering the investigations of non-equilibrium surface exchange and the bulk diffusion of oxygen, a temperature of $T = 500^\circ\text{C}$ for STCC is actually feasible due to the weak temperature dependency of the parameters \tilde{D}_O and \tilde{K}_O . A decrease in the temperature for the re-oxidation step results, e.g., in the decreasing radiation losses of the optical solar concentration system, as well as in the reduced thermal load of the redox material, which is critical regarding the material stability during long-term cycling. Higher reduction extents δ are therefore necessary given the constant reaction conditions. An investigation into the optimal oxygen vacancy concentration of the redox material, e.g., Sm-doped ceria, with a systematic variation in the oxygen non-stoichiometry during the reduction step, is therefore suggested. The use of Zr-doped ceria, on the other hand, as suggested by various authors, has a negative influence. Although Zr-doping enhances the reducibility, surface alteration effects under low-oxygen partial pressure and high temperatures seem to be detrimental to surface exchange kinetics. Moreover, defect interactions are unfavorable in terms of oxygen diffusion at temperatures of $T \leq 800^\circ\text{C}$.

Supplementary Materials: The following are available online at <https://www.mdpi.com/article/10.3390/pr11010109/s1>, Figure S1: Schematic diagram summarising the SIMS IEDP technique for $\sigma < 5\ \mu\text{m}$ (left) and the SIMS IELS technique for $10\ \mu\text{m} < \sigma < h/4$ (right), Figure S2: SIMS line scan depth profile measured in a nominally un-doped polycrystalline ceria as used in this work with the isotope fraction of ^{18}O perpendicular to the original surface, Figure S3: Ion image for ^{18}O tracer exchange of a sectioned sample of nominally un-doped ceria as used in this work, Figure S4: Comparison of two different approaches for the simultaneous determination of D_O and K_O data by applying analytical solutions to the diffusion problem.

Author Contributions: Conceptualization, D.U., L.D., M.S. (Martin Schmücker) and G.B.; Formal analysis, D.U. and L.D.; Funding acquisition, M.R., M.S. (Martin Schmücker) and G.B.; Investigation, D.U., L.D. and M.S. (Michal Schulz); Methodology, L.D., P.F. and G.B.; Project administration, M.R.; Resources, N.K., M.S. (Martin Schmücker) and G.B.; Supervision, M.S. (Martin Schmücker) and G.B.; Visualization, D.U.; Writing—original draft, D.U.; Writing—review and editing, L.D., N.K., P.F., M.R., M.S. (Martin Schmücker) and G.B.. All authors have read and agreed to the published version of the manuscript.

Funding: The authors gratefully acknowledge the financial support from the Deutsche Forschungsgemeinschaft (Grant No. SCHM 1367/5-1 and BOR 532/74-1) as well as by the Helmholtz Association within the Virtual Institute SolarSynGas (VH-VI-509) and the Schöne family foundation.

Data Availability Statement: Not applicable.

Acknowledgments: We would like to thank F. Jomard and C. Argiris for SIMS line scans, S. Fischer for technical assistance with the sample preparation and S. Neitzel-Grieshammer for the helpful discussion.

Conflicts of Interest: The authors declare no conflict of interest.

References

- Chueh, W.C.; Haile, S.M. Ceria as a thermochemical reaction medium for selectively generating syngas or methane from H₂O and CO₂. *ChemSusChem* **2009**, *2*, 735–739. [\[CrossRef\]](#)
- Chueh, W.C.; Falter, C.; Abbott, M.; Scipio, D.; Furler, P.; Haile, S.M.; Steinfeld, A. High-flux solar-driven thermochemical dissociation of CO₂ and H₂O using nonstoichiometric ceria. *Science* **2010**, *330*, 1797–1801. [\[CrossRef\]](#) [\[PubMed\]](#)
- Chueh, W.C.; Haile, S.M. A thermochemical study of ceria: Exploiting an old material for new modes of energy conversion and CO₂ mitigation. *Phil. Trans. R. Soc. A* **2010**, *368*, 3269–3294. [\[CrossRef\]](#)
- Scheffe, J.R.; Steinfeld, A. Thermodynamic Analysis of Cerium-Based Oxides for Solar Thermochemical Fuel Production. *Energy Fuels* **2012**, *26*, 1928–1936. [\[CrossRef\]](#)
- Call, F.; Roeb, M.; Schmücker, M.; Bru, H.; Curulla-Ferre, D.; Sattler, C.; Pitz-Paal, R. Thermogravimetric Analysis of Zirconia-Doped Ceria for Thermochemical Production of Solar Fuel. *Am. J. Anal. Chem.* **2013**, *4*, 37–45. [\[CrossRef\]](#)
- Ackermann, S.; Scheffe, J.R.; Steinfeld, A. Diffusion of Oxygen in Ceria at Elevated Temperatures and Its Application to H₂O/CO₂ Splitting Thermochemical Redox Cycles. *J. Phys. Chem. C* **2014**, *118*, 5216–5225. [\[CrossRef\]](#)
- Call, F.; Roeb, M.; Schmücker, M.; Sattler, C.; Pitz-Paal, R. Ceria Doped with Zirconium and Lanthanide Oxides to Enhance Solar Thermochemical Production of Fuels. *J. Phys. Chem. C* **2015**, *119*, 6929–6938. [\[CrossRef\]](#)
- Ackermann, S.; Sauvin, L.; Castiglioni, R.; Rupp, J.L.M.; Scheffe, J.R.; Steinfeld, A. Kinetics of CO₂ Reduction over Nonstoichiometric Ceria. *J. Phys. Chem. C* **2015**, *119*, 16452–16461. [\[CrossRef\]](#)
- Marxer, D.; Furler, P.; Scheffe, J.; Geerlings, H.; Falter, C.; Batteiger, V.; Sizmann, A.; Steinfeld, A. Demonstration of the Entire Production Chain to Renewable Kerosene via Thermochemical Splitting of H₂O and CO₂. *Energy Fuels* **2015**, *29*, 3241–3250. [\[CrossRef\]](#)
- Lange, M.; Roeb, M.; Sattler, C.; Pitz-Paal, R. Entropy Analysis of Solar Two-Step Thermochemical Cycles for Water and Carbon Dioxide Splitting. *Entropy* **2016**, *18*, 24. [\[CrossRef\]](#)
- Takacs, M.; Ackermann, S.; Bonk, A.; Neises-von Puttkamer, M.; Haueter, P.; Scheffe, J.R.; Vogt, U.F.; Steinfeld, A. Splitting CO₂ with a Ceria-Based Redox Cycle in a Solar-Driven Thermogravimetric Analyzer. *AIChE J.* **2017**, *63*, 1263–1271. [\[CrossRef\]](#) [\[PubMed\]](#)
- Bhosale, R.R.; Takalkar, G.; Sutar, P.; Kumar, A.; AlMomani, F.; Khraisheh, M. A decade of ceria based solar thermochemical H₂O/CO₂ splitting cycle. *Int. J. Hydrogen Energy* **2019**, *44*, 34–60. [\[CrossRef\]](#)
- Belle, J. Oxygen and uranium diffusion in uranium dioxide (a review). *J. Nucl. Mater.* **1969**, *30*, 3–15. [\[CrossRef\]](#)
- Matzke, H.J. On uranium self-diffusion in UO₂ and UO_{2+x}. *J. Nucl. Mater.* **1969**, *30*, 26–35. [\[CrossRef\]](#)
- Ando, K.; Oishi, Y. Diffusion Characteristics of Actinide Oxides. *J. Nucl. Sci. Technol.* **1983**, *20*, 973–982. [\[CrossRef\]](#)
- Matzke, H.J. Diffusion processes and surface effects in non-stoichiometry nuclear fuel oxides UO_{2+x} and (U, Pu)O_{2±x}. *J. Nucl. Mater.* **1983**, *114*, 121–135. [\[CrossRef\]](#)
- Bayoglu, A.; Lorenzelli, R. Oxygen diffusion in f.c.c. fluorite nonstoichiometric nuclear oxides MO_{2±x}. *Solid State Ion.* **1984**, *12*, 53–66. [\[CrossRef\]](#)
- Matzke, H.J. Atomic Transport Properties in UO₂ and mixed Oxides (U, Pu)O₂. *J. Chem. Soc. Faraday Trans.* **1987**, *2*, 1121–1142. [\[CrossRef\]](#)
- Abanades, S.; Flamant, G. Thermochemical hydrogen production from a two-step solar-driven water-splitting cycle based on cerium oxides. *Sol. Energy* **2006**, *80*, 1611–1623. [\[CrossRef\]](#)
- Blumenthal, R.N.; Lee, P.W.; Panlener, R.J. Studies on the Defect Structure on Nonstoichiometric Cerium Dioxide. *J. Electrochem. Soc.* **1971**, *118*, 123–129. [\[CrossRef\]](#)
- Tuller, H.L.; Nowick, A.S. Small polaron electron transport in reduced CeO₂ single crystals. *J. Phys. Chem. Solids* **1977**, *38*, 859–867. [\[CrossRef\]](#)
- Wang, D.Y.; Nowick, A.S. The “grain-boundary effect” in doped ceria solid electrolytes. *J. Solid State Chem.* **1980**, *35*, 325–333. [\[CrossRef\]](#)
- Hohnke, D.K. Ionic conduction in doped oxides with the fluorite structure. *Solid State Ion.* **1981**, *5*, 531–534. [\[CrossRef\]](#)
- Faber, J.; Geoffroy, C.; Roux, A.; Sylvestre, A.; Abelard, P. A systematic investigation of the dc electrical conductivity of rare-earth doped ceria. *Appl. Phys. A* **1989**, *49*, 225–232. [\[CrossRef\]](#)
- Eguchi, K.; Setoguchi, T.; Inoue, T.; Arai, H. Electrical properties of ceria-based oxides and their application to solid oxide fuel cells. *Solid State Ion.* **1992**, *52*, 165–172. [\[CrossRef\]](#)
- Mogensen, M.; Sammes, N.M.; Tompsett, G.A. Physical, chemical and electrochemical properties of pure and doped ceria. *Solid State Ion.* **2000**, *129*, 63–94. [\[CrossRef\]](#)
- Tianshu, Z.; Hing, P.; Huang, H.; Kilner, J.A. Ionic conductivity in the CeO₂-Gd₂O₃ system (0.05 ≤ Gd/Ce ≤ 0.4) prepared by oxalate coprecipitation. *Solid State Ion.* **2002**, *148*, 567. [\[CrossRef\]](#)
- Feng, Z.A.; Gabaly, F.E.; Ye, X.; Shen, Z.-X.; Chueh, W.C. Fast vacancy-mediated oxygen ion incorporation across the ceria-gas electrochemical interface. *Nat. Commun.* **2014**, *5*, 4374–4382. [\[CrossRef\]](#)
- Pullar, R.C.; Novais, R.M.; Caetano, A.P.F.; Barreiros, M.A.; Abanades, S.; Costa Oliveira, F.A. A Review of Solar Thermochemical CO₂ Splitting Using Ceria-Based Ceramics with Designed Morphologies and Microstructures. *Front. Chem.* **2019**, *7*, 601. [\[CrossRef\]](#)

30. Knoblauch, N.; Dörrer, L.; Fielitz, P.; Schmücker, M.; Borchardt, G. Surface controlled reduction kinetics of nominally undoped polycrystalline CeO₂. *Phys. Chem. Chem. Phys.* **2015**, *17*, 5849–5860. [\[CrossRef\]](#)
31. Knoblauch, N.; Simon, H.; Dörrer, L.; Uxa, D.; Fielitz, P.; Wendelstorf, J.; Spitzer, K.-H.; Schmücker, M.; Borchardt, G. Ceria: Recent Results on Dopant-Induced Surface Phenomena. *Inorganics* **2017**, *5*, 76. [\[CrossRef\]](#)
32. Hahn, K.R.; Iannuzzi, M.; Seitsonen, A.P.; Hutter, J. Coverage Effect of the CO₂ Adsorption Mechanisms on CeO₂(111) by First Principles Analysis. *J. Phys. Chem. C* **2013**, *117*, 1701–1711. [\[CrossRef\]](#)
33. Cheng, Z.; Sherman, B.J.; Lo, C.S. Carbon dioxide activation and dissociation on ceria(110): A density functional theory study. *J. Chem. Phys.* **2013**, *138*, 014702–014714. [\[CrossRef\]](#)
34. Pechini, M.P. Method of preparing lead and alkaline earth titanates and niobates and coating method using the same to form a capacitor. U.S. Patent 3.330.697, 11 July 1967.
35. Fielitz, P.; Borchardt, G. On the accurate measurement of oxygen self-diffusivities and surface exchange coefficients in oxides via SIMS depth profiling. *Solid State Ion.* **2001**, *144*, 71–80. [\[CrossRef\]](#)
36. Kilner, J.A.; Steele, B.C.H. Oxygen self-diffusion studies using negative-ion secondary ion mass spectrometry (SIMS). *Solid State Ion.* **1984**, *12*, 89–97. [\[CrossRef\]](#)
37. Chater, R.J.; Carter, S.; Kilner, J.A.; Steele, B.C.H. Development of a novel SIMS technique for oxygen self-diffusion and surface exchange coefficient measurements in oxides of high diffusivity. *Solid State Ion.* **1992**, *53–56*, 859–867. [\[CrossRef\]](#)
38. Bevan, D.J.M.; Kordis, J. Mixed oxides of the type MO₂ (fluorite)-M₂O₃-I. Oxygen dissociation pressures and phase relationships in the system CeO₂-Ce₂O₃ at high temperatures. *J. Inorg. Nucl. Chem.* **1964**, *26*, 1509–1523. [\[CrossRef\]](#)
39. Panlener, R.J.; Blumenthal, R.N.; Ganier, J.E. A thermodynamic study of nonstoichiometric cerium oxide. *J. Phys. Chem. Solids* **1975**, *36*, 1213–1222. [\[CrossRef\]](#)
40. Crank, J. *The Mathematics of Diffusion*, 2nd ed.; Oxford University Press: Oxford, UK, 1975.
41. Kilner, J.A.; De Souza, R.A.; Fullarton, I.C. Surface exchange of oxygen in mixed conducting perovskite oxides. *Solid State Ion.* **1996**, *86–88*, 703–709. [\[CrossRef\]](#)
42. Fischer, E.; Hertz, J.L. Measurability of the diffusion and surface exchange coefficients using isotope exchange with thin film and traditional samples. *Solid State Ion.* **2012**, *218*, 18–24. [\[CrossRef\]](#)
43. Manning, P.S.; Sirman, J.D.; Kilner, J.A. Oxygen self-diffusion and surface exchange studies of oxide electrolytes having the fluorite structure. *Solid State Ion.* **1997**, *93*, 125–132. [\[CrossRef\]](#)
44. Maier, J. Interaction of oxygen with oxides: How to interpret measured effective rate constants? *Solid State Ion.* **2000**, *135*, 575–588. [\[CrossRef\]](#)
45. De Souza, R.A. A universal empirical expression for the isotope surface exchange coefficients (*k*^{*}) of acceptor-doped perovskite and fluorite oxides. *Phys. Chem. Chem. Phys.* **2006**, *8*, 890–897. [\[CrossRef\]](#)
46. Schaub, M.; Merkle, R.; Maier, J. Interdependence of Point Defects and Reaction Kinetics: CO and CH₄ Oxidation on Ceria and Zirconia. *J. Phys. Chem. C* **2020**, *124*, 18544–18556. [\[CrossRef\]](#)
47. Kroeger, F.A.; Vink, H.J. Relations between Concentrations of Imperfections in Crystalline Solids. In *Solid State Physics*; Seitz, F., Turnbull, D., Eds.; Academic Press: New York, NY, USA, 1956; Volume 3, pp. 307–435.
48. Chueh, W.C.; McDaniel, A.H.; Grass, M.E.; Hao, Y.; Jabeen, N.; Liu, Z.; Haile, S.M.; McCarty, K.F.; Bluhm, H.; El Gabaly, F. Highly Enhanced Concentration and Stability of Reactive Ce³⁺ on Doped CeO₂ Surface Revealed In Operando. *Chem. Mater.* **2012**, *24*, 1876–1882. [\[CrossRef\]](#)
49. Zhao, Z.; Uddi, M.; Tsvetkov, N.; Yildiz, B.; Ghoniem, A.F. Redox Kinetics Study of Fuel reduced Ceria for Chemical-Looping Water Splitting. *J. Phys. Chem. C* **2016**, *120*, 16271–16289. [\[CrossRef\]](#)
50. Zhang, C.; Grass, M.E.; Yu, Y.; Gaskell, K.J.; DeCaluwe, S.C.; Chang, R.; Jackson, G.S.; Hussain, Z.; Bluhm, H.; Eichhorn, B.W.; et al. Multielement Activity Mapping and Potential Mapping in Solid Oxide Electrochemical Cells through the use of operando XPS. *ACS Catal.* **2012**, *2*, 2297–2304. [\[CrossRef\]](#)
51. Yu, Y.; Mao, B.; Geller, A.; Chang, R.; Gaskell, K.; Liu, Z.; Eichhorn, B.W. CO₂ activation and carbonate intermediates: An operando AP-XPS study of CO₂ electrolysis reactions on solid oxide electrochemical cells. *Phys. Chem. Chem. Phys.* **2014**, *16*, 11633–11639. [\[CrossRef\]](#)
52. Feng, Z.; Machala, M.L.; Chueh, W.C. Surface electrochemistry of CO₂ reduction and CO oxidation on Sm-doped CeO_{2-x}: Coupling between Ce³⁺ and carbonate adsorbates. *Phys. Chem. Chem. Phys.* **2015**, *17*, 12273–12281. [\[CrossRef\]](#)
53. Fielitz, P.; Borchardt, G. Oxygen exchange at gas/solid interfaces: How the apparent activation energy of the surface exchange coefficient depends on the kinetic regime. *Phys. Chem. Chem. Phys.* **2016**, *18*, 22031–22038. [\[CrossRef\]](#)
54. Muhich, C.L. Re-Evaluating CeO₂ Expansion Upon Reduction: Non-counterpoised Forces, Not Ionic Radius Effects, Are the Cause. *J. Phys. Chem. C* **2017**, *121*, 8052–8059. [\[CrossRef\]](#)
55. Grieshammer, S. Defect Interactions in the CeO₂-ZrO₂-Y₂O₃ Solid Solution. *J. Phys. Chem. C* **2017**, *121*, 15078–15084. [\[CrossRef\]](#)
56. Grieshammer, S.; Eisele, S.; Koettgen, J. Modeling Oxygen Ion Migration in the CeO₂-ZrO₂-Y₂O₃ Solid Solution. *J. Phys. Chem. C* **2018**, *122*, 18809–18817. [\[CrossRef\]](#)
57. Eufinger, J.-P.; Daniels, M.; Schmale, K.; Berendts, S.; Ulbrich, G.; Lerch, M.; Wiemhöfer, H.-D.; Janek, J. The model case of an oxygen storage catalyst—Non-stoichiometry, point defects and electrical conductivity of single crystalline CeO₂-ZrO₂-Y₂O₃ solid solutions. *Phys. Chem. Chem. Phys.* **2014**, *16*, 25583–25600. [\[CrossRef\]](#)

58. Bishop, S.R.; Duncan, K.L.; Wachsman, E.D. Defect equilibria and chemical expansion in nonstoichiometric undoped and gadolinium-doped cerium oxide. *Electrochim. Acta* **2009**, *54*, 1436–1443. [[CrossRef](#)]
59. Bishop, S.R.; Duncan, K.L.; Wachsman, E.D. Surface and bulk oxygen non-stoichiometry and bulk expansion in gadolinium-doped cerium oxide. *Acta Mater.* **2009**, *57*, 3596–3605. [[CrossRef](#)]
60. Claus, J.; Leonhardt, M.; Maier, J. Tracer diffusion and chemical diffusion of oxygen in acceptor doped SrTiO₃. *J. Phys. Chem. Solids* **2000**, *61*, 1199–1207. [[CrossRef](#)]

Disclaimer/Publisher’s Note: The statements, opinions and data contained in all publications are solely those of the individual author(s) and contributor(s) and not of MDPI and/or the editor(s). MDPI and/or the editor(s) disclaim responsibility for any injury to people or property resulting from any ideas, methods, instructions or products referred to in the content.